

Dynamical Tuning of Energy Transfer Efficiency on a Graphene Monolayer

Vasilios D. Karanikolas, Cristian A. Marocico, and A. Louise Bradley

Semiconductor Photonics Group, School of Physics and CRANN,

Trinity College Dublin, College Green 2, Dublin, Ireland

(Dated: October 23, 2018)

We present in this contribution a theoretical investigation of the spontaneous emission and energy transfer rates between quantum systems placed above a monolayer of conducting graphene. The conditions for strong and weak coupling between a quantum system and the surface plasmon-polariton of graphene are determined and, subsequently, we focus exclusively on the weak coupling regime. We then calculate the dispersion relation of the surface plasmon mode on graphene and, by varying the chemical potential, show a good control of its resonance frequency. Using a Green's tensor formalism, we calculate the spontaneous emission and energy transfer rates of quantum systems placed near the graphene monolayer. The spontaneous emission rate of a single quantum system is enhanced by several orders of magnitude close to the graphene monolayer and we show that this enhancement is due almost exclusively to excitation of the surface plasmon mode. When considering the energy transfer rate between two quantum systems, we find a similar enhancement of several orders of magnitude close to the graphene monolayer. The direct interaction between the donor and acceptor dominates when they are close to each other, but is modified from its free-space behavior due to the presence of the graphene monolayer. As the donor-acceptor separation is increased, their direct interaction is overshadowed by the interaction via the surface plasmon mode. Due to the large propagation length of surface plasmon mode on graphene – hundreds of nanometers – this enhancement of the energy transfer rate holds over large donor-acceptor separations along the graphene monolayer.

PACS numbers: 33.80.-b

I. INTRODUCTION

For the last two decades the field of plasmonics has grown intensively. Confining light to sub-wavelength structures by exciting surface plasmon-polariton (SPP) modes has various applications in biosensing devices, light harvesting, optical nanoantennas and quantum information processing. SPPs are collective oscillations of electrons and the electromagnetic field that are excited at the interface between a dielectric and a conductor and can propagate along that interface.¹ In plasmonics, noble metals are routinely used as the conducting medium. The main drawback of using noble metals in the applications mentioned above is their large Ohmic losses.²

Graphene constitutes an alternative to using noble metals for plasmonic applications.^{3–7} It is a two-dimensional material possessing unique properties. This atomically thick monolayer has superior electronic and mechanical properties originating in part from its charge carriers of zero effective mass that can travel for microns without scattering at room temperatures.⁸

An undoped graphene monolayer (GM) can absorb $\pi\alpha_0 \approx 2.3\%$ of the light incident upon it, where α_0 is the fine structure constant.⁹ Patterned GM nanostructures can give rise to 100% absorption at specific wavelengths, which can be tuned through the applied voltage.^{10–12}

Interactions between quantum emitters (QEs) and a GM have been investigated intensively over the last few years, especially as regards the influence of the GM on the spontaneous emission (SE) rate of a QE placed near the GM.^{13–17} It has been found that the SE rate can be enhanced by several order of magnitude compared with its free space value, due to the excitation of graphene plasmon (GP) modes. Furthermore, confinement of the GP modes to one dimension (graphene ribbons)^{12,15} and zero dimensions (graphene

nanodisks)^{11,15,18} can enhance the QE-GM interaction even more. In the case of zero-dimensional confinement, the strong-coupling regime can be achieved between a QE and graphene nanodisks.¹⁵

The presence of a second QE in the system will modify the emission properties of the system, giving rise to super- and sub-radiant states.^{19,20} Once more, the confinement of the GP to one dimension (graphene ribbons)²¹ or zero dimensions (graphene nanodisks)¹⁸ further enhances the interaction rates. The energy transfer (ET) rate between a pair of QEs has also been investigated in the presence of a GM.²²

In this contribution we investigate the SE and ET rates of quantum emitters placed near a graphene layer using a semi-analytical Green's tensor formalism.²³ We use quantum emitters with optical properties corresponding to real physical systems. The SE and ET rates are competitive processes, thus an ET efficiency is introduced. This quantity, which is a measure of the contribution of the energy transfer rate to the total decay rate of the donor, shows that one can efficiently transfer energy between QEs separated by distances of the order of hundreds of nanometers, due to the excitation of GP modes on the GM. The ET efficiency can be tuned, through gating of the GM, thus opening opportunities for applications such as switching and sensing devices,^{24–26} light harvesting,²⁷ plasmonic rulers^{25,28} and quantum computing.²⁹ Furthermore we show that the ET rate along the GM has two contributions, a Förster contribution, and a GP contribution, both of which can be tuned. We also show that the ET rate perpendicular to the GM is mainly characterized by the penetration depth of the GP mode.

The paper is structured as follows. We begin in Sec. II with a theoretical framework in which we introduce the optical properties of the GM and the GP mode it supports (Sec. II A), and we also investigate the different coupling regimes of the

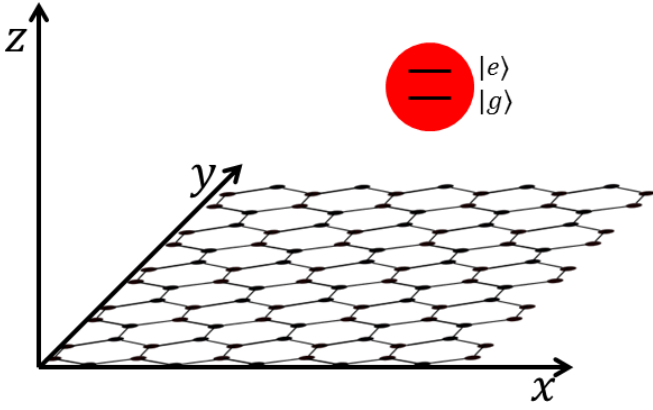


Figure 1: (Color online) A graphene monolayer in the xy -plane, with the quantum emitter approximated as a two level system.

QE-GM system, i.e. strong or weak coupling (Sec. II B). In Sec. III we present the results of our calculations for the SE rate (Sec. III A), the ET function (Sec. III B) and the ET efficiency (Sec. III C), for different distance regimes and values of the chemical potential. Finally, in Sec. IV we give a summary of the results and the conclusions drawn. In addition, we include two Appendixes where we present various expressions used in the main body of the paper.

II. THEORETICAL FRAMEWORK

The model system considered in this paper is presented as a sketch in Fig. 1. We consider an atomically thin monolayer of graphene in the xy -plane, suspended in vacuum. Close to this graphene monolayer, we have either a single quantum system, when investigating spontaneous emission, or two quantum systems, for energy transfer investigations. We begin our investigation by considering a conductivity model for graphene and the GP properties.

A. Graphene Conductivity and GP Properties

We calculate the graphene in-plane conductivity, σ , in the random phase approximation (RPA).^{30–32} This quantity is mainly controlled by electron-hole pair excitation that can be divided into intraband and interband excitations. It can be written as

$$\sigma = \sigma_{\text{intra}} + \sigma_{\text{inter}}, \quad (1)$$

where the intraband and interband contributions are,

$$\sigma_{\text{intra}} = \frac{2ie^2t}{\hbar\pi(\Omega + i\gamma)} \ln \left[2 \cosh \left(\frac{1}{2t} \right) \right], \quad (2)$$

$$\sigma_{\text{inter}} = \frac{e^2}{4\hbar} \left[\frac{1}{2} + \frac{1}{\pi} \arctan \left(\frac{\Omega - 2}{2t} \right) - \frac{i}{2\pi} \ln \frac{(\Omega + 2)^2}{(\Omega - 2)^2 + (2t)^2} \right]. \quad (3)$$

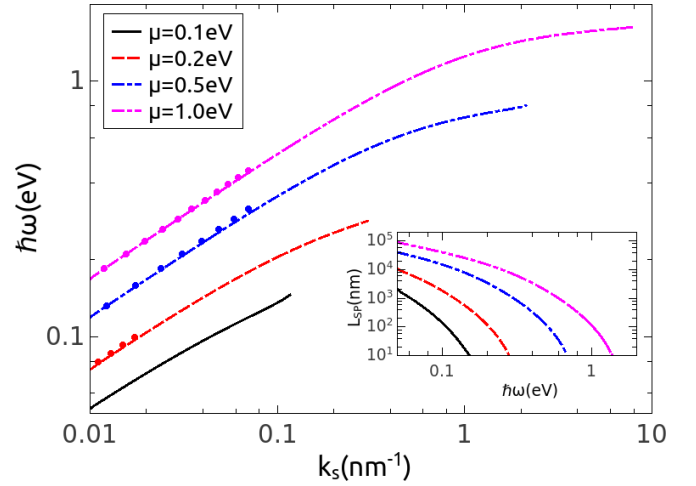


Figure 2: (Color online) GP dispersion relation in doped graphene, $\hbar\omega(k_s)$, for different values of the chemical potential μ ; the dots show the quadratic approximation of the dispersion relation. The inset shows the propagation length of the GP mode, L_{SP} , for the same values of the chemical potential, μ .

In the above we have introduced the dimensionless parameters $\Omega = \hbar\omega/\mu$, $\gamma = E_S/\mu$ and $t = k_B T/\mu$. Here, μ is the chemical potential, T is the temperature, and E_S is the scattering energy. This scattering energy is related to the relaxation time τ through $\tau = \hbar/E_S$. The σ_{intra} term describes a Drude model response for intraband processes corrected with a term γ , which accounts for impurities compromising the electron's mobility. Throughout this paper we consider a temperature $T = 300$ K and a value of the relaxation time of $\tau = 1$ ps.^{33,34} Fig. 2 shows the dispersion relation, $\omega(k_s)$, for different values of the chemical potential, μ . Due to the fact that retardation effects dominate for wavevectors $k_s > k_F$ and energies $\hbar\omega > 2\mu$, the GP dispersion curves in Fig. 2 terminate at these values, where k_F is the Fermi wavevector. When the chemical potential, μ , has the value $\mu = 0$, the GM absorbance has the value $\pi\alpha_0 \approx 2.3\%$, where α_0 is the fine structure constant. This is the asymptotic value of the doped GM for energies $\hbar\omega > 2\mu$. Considering that the GM is surrounded by air, $\epsilon_1 = \epsilon_2 = 1$ (free standing GM), the GP dispersion relation can be obtained form:

$$\frac{1}{\sqrt{k_0^2 - k_{SP}^2}} = -\frac{2\pi\sigma}{\omega}, \quad (4)$$

where k_{SP} is the GP wavevector.¹⁵ Because $k_{SP} \gg k_0$, we can simplify the dispersion relation above, using only the σ_{intra} contribution, to obtain

$$k_{SP} = \frac{\hbar^2}{4e^2\mu k_B T \ln \left[2 \cosh \left(\frac{\mu}{k_B T} \right) \right]} \omega \left(\omega + \frac{i}{\tau} \right), \quad (5)$$

which has as its main feature the quadratic dependence of the GP wavevector on the frequency, when the intraband contributions dominate.³⁰ This approximate quadratic dependence

is shown as dots in Fig. 2. Another feature of the GP dispersion relation on graphene is the fact that the GP resonance frequency is blue-shifted as the chemical potential increases.

The inset in Fig. 2 shows the propagation length of the surface plasmon along the graphene, $L_{SP} = 1/\text{Im}(k_s)$, as a function of energy, for different values of the chemical potential, μ . It is evident from the plot that, depending on the value of the chemical potential, μ , this propagation length can reach values as large as hundreds of microns at low frequencies. As the energy is increased, however, the propagation length decreases rapidly, because the GP then has sufficient energy to generate electron-hole pairs and the dispersion relation is dominated by the interband contributions.³

B. Rabi splitting - strong coupling regime

In order to ascertain whether the weak or strong coupling regime applies for particular sets of parameters, we now consider a model consisting of a single QE interacting with the GP mode of the GM. To describe this system, we use a Jaynes-Cummings Hamiltonian³⁵ of the form:

$$H = \frac{\hbar\omega}{2}\sigma_z + \hbar\omega_{SP}\hat{a}^\dagger\hat{a} + \hbar g(\hat{a}\sigma_+ + \hat{a}^\dagger\sigma_-), \quad (6)$$

where ω_{SP} is the GP frequency, \hat{a}^\dagger and \hat{a} are the creation and annihilation operators of the plasmon mode, ω is the transition frequency of the QE between its ground and excited state, σ_+ and σ_- are the raising and lowering operators of the QE, and g is the coupling constant between the QE and the GP mode of the GM. The coupling constant g is given by³⁶

$$\begin{aligned} |g(\omega)|^2 &= \frac{1}{\hbar\pi\epsilon_0} \frac{\omega^2}{c^2} \hat{\mathbf{d}}^T \text{Im}\mathfrak{G}_{SP}(\omega, \mathbf{r}_{QE}, \mathbf{r}_{QE}) \hat{\mathbf{d}} \\ &= \gamma_0 \frac{3c}{\omega} \hat{\mathbf{d}}^T \text{Im}\mathfrak{G}_{SP}(\omega, \mathbf{r}_{QE}, \mathbf{r}_{QE}) \hat{\mathbf{d}}, \end{aligned} \quad (7)$$

where $\mathfrak{G}_{SP}(\omega, \mathbf{r}_{QE}, \mathbf{r}_{QE})$ is the GP part of the Green's tensor, derived in Appendix A, Eq. (A2a), γ_0 is the Einstein A-coefficient, $\gamma_0 = \omega^3 d^2 / (3\pi\hbar\epsilon_0 c^3)$ and \mathbf{d} is the transition dipole moment of the QE positioned at $\mathbf{r}_{QE} = (0, 0, z)$. In this section, we consider $\gamma_0 = 5 \times 10^{-8} \text{ fs}^{-1}$ and we consider the transition dipole moment, \mathbf{d} , of the QE to be oriented along z . Since we are interested in the coupling between the GP mode and the QE we calculate the GP contribution to Eq. (A2a), by extracting the pole contribution and we obtain

$$\mathfrak{G}_{S,zz}^{(11)SP}(z, \omega) = -\frac{1}{4} \frac{(1 - 1/\alpha^2)}{\alpha k_0} e^{-2iz/\alpha}, \quad (8)$$

where $\alpha = 2\pi\sigma/c$.

The Hamiltonian from Eq. (6) couples the states $|e\rangle \otimes |0\rangle$ and $|g\rangle \otimes |1\rangle$ to the dressed states $|1\rangle$ and $|2\rangle$ with energies,

$$E_1 = \frac{\hbar\omega_{SP}}{2} - \frac{\hbar}{2} \sqrt{\delta^2 + 4g^2}, \quad (9a)$$

$$E_2 = \frac{\hbar\omega_{SP}}{2} + \frac{\hbar}{2} \sqrt{\delta^2 + 4g^2}, \quad (9b)$$

where $\delta = \omega_{SP} - \omega$, is the detuning between the GP mode resonant frequency and the transition frequency of the QE. The energy states are separated by $\Omega = \sqrt{\delta^2 + 4g^2}$, which gives the value of the Rabi splitting. As an example, if we consider the case where the QE is positioned at $z = 10 \text{ nm}$ above a GM with a chemical potential equal to the transition energy of the QE, $\mu = \hbar\omega = 0.5 \text{ eV}$, the Rabi splitting, at $\delta = 0$, has a value $2g(\omega) = 0.12 \text{ eV}$.

In order to further investigate the weak and strong coupling regimes, we will analyze the dependence of the coupling constant, g , on the various parameters involved, namely the value of the chemical potential, μ , the emission frequency of the QE, ω , and the distance of the QE to the GM, z . Considering $\omega = \omega_{SP}$, i.e. zero detuning, the criterion for having strong coupling is whether or not the absorption spectrum of the system exhibits two peaks of different frequencies.^{36,37} This condition is fulfilled if

$$|g| > \frac{1}{4} |\chi_{LSW} - \kappa|, \quad (10)$$

where χ_{LSW} represents the *lossy surface waves* (LSW) contribution, which are non-propagating evanescent modes relaxing through Ohmic losses, and κ is the width of the $g(\omega)^2$ spectrum.

In Fig. 3a we present a contour plot of the quantity $\mathfrak{D} = 4|g|/|\chi_{LSW} - \kappa|$ as a function of the chemical potential, μ , and the emission energy, $\hbar\omega$, for a fixed position of the QE, $z = 10 \text{ nm}$. Although from condition (10) when $\mathfrak{D} < 1$ we are in the weak coupling regime, this condition might not be sufficient under some experimental conditions,³⁵ and we thus consider the more stringent inequality $\mathfrak{D} \lesssim 0.5$ as giving the weak coupling condition. As is evident from Fig. 3a, for chemical potential values $\mu < 0.3 \text{ eV}$, there exists a frequency region where we have $\mathfrak{D} \geq 0.5$ and the weak coupling approximation needed to calculate the SE and ET rates is no longer valid. This region where the strong coupling dominates corresponds to THz frequencies, a range outside the scope of our investigation. For chemical potential values $\mu > 0.6 \text{ eV}$, on the other hand, the quantity \mathfrak{D} has values below 0.2, at all frequencies, well within the weak-coupling regime.

Fig. 3b examines the maximum value of \mathfrak{D} for different values of the chemical potential, μ , and at different positions of the QE above the QM. For each point, we calculate the maximum value of \mathfrak{D} as a function of the emission energy of the QE, $\hbar\omega$. This represents, therefore, the worst-case scenario for weak coupling, since at all other frequencies, \mathfrak{D} will be smaller than the values depicted in Fig. 3b. It can be seen that the SC regime is only accessed for values of $\mu < 0.4 \text{ eV}$ at certain frequencies. Throughout the rest of the paper we only consider frequencies ranges which remain outside the SC regime for all values of μ and g explored.

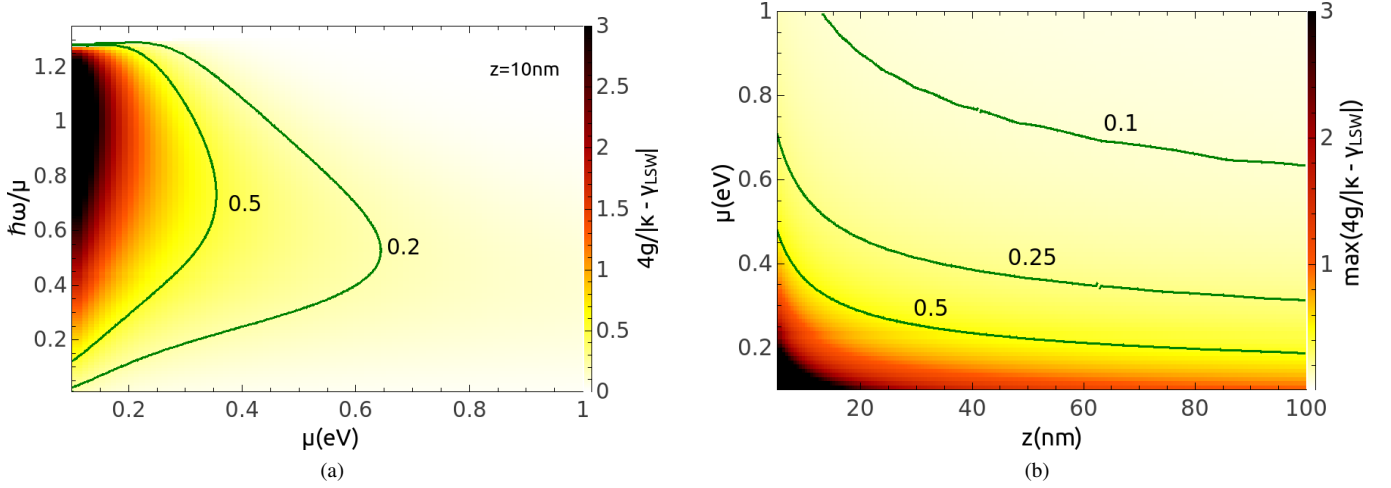


Figure 3: (Color online) Contour plots of the quantity $\mathfrak{D} = 4|g|/|\gamma_{LSW} - \kappa|$ as a function of (a) chemical potential, μ , and emission energy, $\hbar\omega$ normalized by the chemical potential, for fixed QE position $z = 10$ nm, (b) chemical potential, μ , and QE position, z ; each point reflects the maximum value of $\mathfrak{D}(\omega)$.

III. RESULTS AND DISCUSSION

A. Spontaneous emission rate

The decay rate γ is proportional to the strength of the coupling between the transition dipole matrix element and the electromagnetic modes acting on it. The normalized SE has the expression²³

$$\tilde{\gamma} = \frac{\gamma}{\gamma_0} = n_i + \frac{6\pi c}{\omega} \text{Im}[\mathbf{n}_{QE} \cdot \mathfrak{S}_s(\mathbf{r}, \mathbf{r}, \omega) \cdot \mathbf{n}_{QE}], \quad (11)$$

where γ_0 is Einstein's A-coefficient, \mathbf{n}_{QE} is a unit vector along the direction of the transition dipole moment of the emitter, and $\mathfrak{S}(\mathbf{r}, \mathbf{r}, \omega)$ is given by (A2).

In Fig. 4a we have plotted the normalized SE rate, $\tilde{\gamma}$, of a QE at a fixed position, $\mathbf{r} = (0, 0, 10 \text{ nm})$ above the GM, as a function of the QE's emission energy, $\hbar\omega$, for different values of the chemical potential, μ . In general the SE rate has a peak at an energy below μ . As the energy is further increased, the SE rate drops dramatically before finally recovering to a value independent of μ , when the energy is above 2μ . As we increase the value of μ , the GP peak blue-shifts and is broadened, and its value decreases. The general drop in the SE rate is most visible starting with values of the chemical potential of $\mu > 0.4 \text{ eV}$, and it occurs between the energies $\hbar\omega = \mu$ and $\hbar\omega = 2\mu$. This drop is due to interband transitions when the QE relaxes through lossy channels. At emission energies $\hbar\omega > 2\mu$ the emission is determined by interband contributions and GP excitations become unimportant, as the dispersion relations in Fig. 2 show. At these energies the SE rate follows the same behavior as for the case of undoped graphene, $\mu = 0 \text{ eV}$, as seen in Fig. 4a. Moreover, we can see that the main contribution to the peak in the normalized SE rate, $\tilde{\gamma}$, comes from the GP contribution, which is denoted by the circular symbols in Fig. 4a. The maximum value of \mathfrak{D} is 0.41 at

$\mu = 0.4 \text{ eV}$, thus placing us within the weak coupling regime.

B. Energy transfer function

In this section we investigate the influence of the GM on the energy transfer process between a pair of QEs, a donor and an acceptor. The normalized energy transfer function which we investigate in this section is given as

$$\tilde{\Gamma} = \frac{\Gamma}{\Gamma_0} = \frac{|\mathbf{n}_A \cdot \mathfrak{S}(\mathbf{r}_A, \mathbf{r}_D, \omega) \cdot \mathbf{n}_D|^2}{|\mathbf{n}_A \cdot \mathfrak{S}_0(\mathbf{r}_A, \mathbf{r}_D, \omega) \cdot \mathbf{n}_D|^2}, \quad (12)$$

(see also (B5)).

Fig. 4b shows the normalized energy transfer function, $\tilde{\Gamma}$, as a function of frequency for different values of the chemical potential, μ , and when both the donor and acceptor transition dipole moments are oriented perpendicular to the GM, i.e. zz -orientation. The donor and acceptor positions are fixed at $\mathbf{r}_D = (0, 0, 10 \text{ nm})$ and $\mathbf{r}_A = (100 \text{ nm}, 0, 10 \text{ nm})$, respectively. As for the case of the SE rate in 4a, the normalized ET function, $\tilde{\Gamma}$, is enhanced close to the GP frequency and in general for frequencies $\hbar\omega < \mu$, where the intraband transitions dominate. For frequencies $\hbar\omega > \mu$ the energy transfer rate decreases due to the losses generated by the interband contributions.

Fig. 5 presents contour plots of the normalized ET function, $\tilde{\Gamma}$, as a function of the position of the acceptor in (a) the xz -plane and (b) the xy -plane 10 nm above the GM, when the donor position is fixed at $\mathbf{r}_D = (0, 0, 10 \text{ nm})$, the transition energy is $\hbar\omega = 0.52 \text{ eV}$ ($\lambda = 2.3 \mu\text{m}$) and the chemical potential is $\mu = 1.0 \text{ eV}$. In Fig. 5a the normalized ET function has large values when the acceptor is close to the GM and decreases as the acceptor distance is increased. This behavior is due to the fact that the field is highly confined in the z -direction at the surface of the GM, with a penetration depth of $\delta_{SP} = 10 \text{ nm}$, or

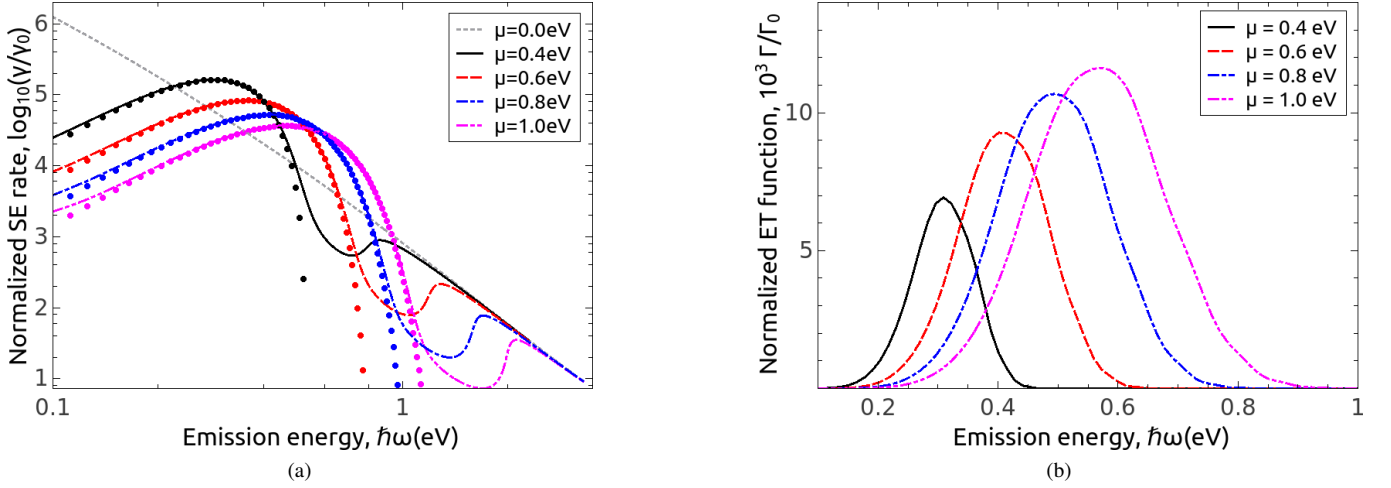


Figure 4: (Color online) (a) SE rate of a QE, positioned at $\mathbf{r} = (0, 0, 10 \text{ nm})$, as a function of its emission frequency for different values of the chemical potential, μ . (b) Normalized ET function, $\tilde{\Gamma}(\mathbf{r}_A, \mathbf{r}_D, \omega)$, between a donor and acceptor QE as a function of frequency, for fixed donor and acceptor positions, $\mathbf{r}_D = (0, 0, 10 \text{ nm})$ and $\mathbf{r}_A = (100 \text{ nm}, 0, 10 \text{ nm})$ respectively, and different values of the chemical potential, μ .

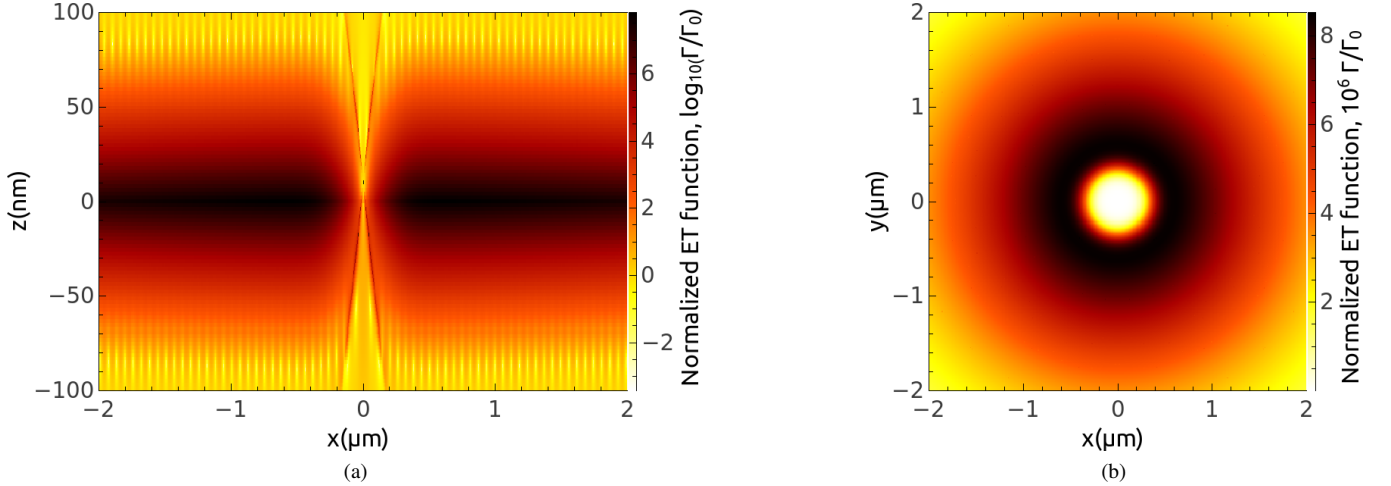


Figure 5: (Color online) Contour plots of the normalized ET function, in the (a) xz -plane and (b) xy -plane when $z = 10 \text{ nm}$, for a donor positioned at $\mathbf{r}_D = (0, 0, 10 \text{ nm})$ above a GM. The dielectric permittivity of the surrounding media is $\epsilon_1 = \epsilon_2 = 1$. The chemical potential of the graphene monolayer is $\mu = 1.0 \text{ eV}$. The emission frequency of the donor is $\omega = 0.8 \text{ fs}^{-1}$ ($\lambda = 2.3 \mu\text{m}$). Both donor and acceptor have their transition dipole moments oriented along the z -axis.

$\delta_{\text{SP}}/\lambda = 4 \cdot 10^{-3}$. The fringes visible in Fig. 5a are due to the constructive and destructive interference between the direct and scattering terms in the Green's tensor, cf Eq. (A1). This effect is more profound due to the dipole moment orientations of the QEs, along the z -axis. Fig. 5b shows that the normalized ET function has cylindrical symmetry in the xy -plane, due to the orientation of both donor and acceptor transition dipole moments along the z -axis. Furthermore, we see that the normalized ET function has a peak value at a distance of about 400 nm, which is the propagation length of the GP mode for the particular set of parameters used in this calculation.

In Fig. 6a we present the z -dependence of the normalized

ET function, $\tilde{\Gamma}$, for a donor located at $\mathbf{r}_D = (0, 0, z)$ and an acceptor at $\mathbf{r}_A = (100 \text{ nm}, 0, z)$, for various values of the chemical potential, and a fixed transition energy, $\hbar\omega = 0.33 \text{ eV}$. As we have already pointed out, for different values of the chemical potential, μ , the position of the maximum in the normalized ET function blueshifts as the value of the chemical potential is increased, cf. Fig. 4b. Thus, for the smallest value of the chemical potential, $\mu = 0.2 \text{ eV}$, the enhancement of the ET function is negligible to non-existent. As the value of the chemical potential is increased, the ET function has values a few orders of magnitude larger than in free-space when the donor-acceptor pair is close to the GM. As the donor-acceptor

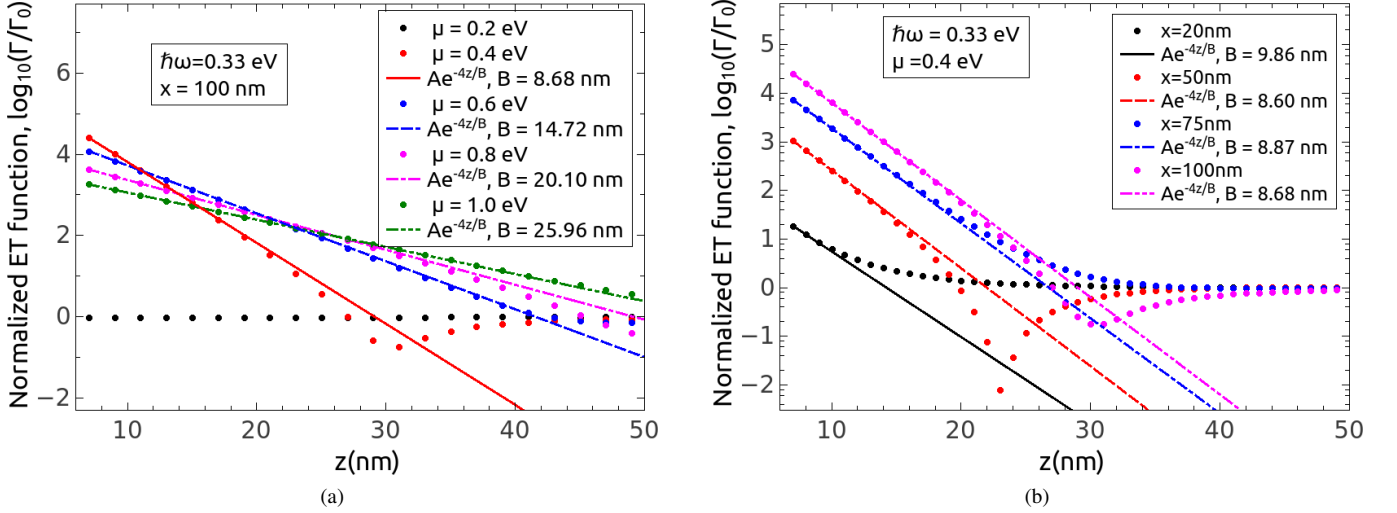


Figure 6: (Color online) Normalized ET function, $\tilde{\Gamma}(\mathbf{r}, \mathbf{s}, \omega)$, as a function of the donor and acceptor distance to the graphene monolayer, for a fixed transition energy, $\hbar\omega = 0.33$ eV. (a) For various values of the chemical potential, μ , when the donor position is $\mathbf{r}_D = (0, 0, z)$ and the acceptor position is $\mathbf{r}_A = (100 \text{ nm}, 0, z)$; (b) For various in-plane distances, x , when the donor position is $\mathbf{r}_D = (0, 0, z)$ and the acceptor position is $\mathbf{r}_A = (x, 0, z)$, for a fixed value of the chemical potential, $\mu = 0.4$ eV. The symbols represent the full simulation data, while the lines are fits with the exponential function in the legend. Both donor and acceptor have their transition dipole moments oriented along the z -axis.

Table I:

$\hbar\omega$ (eV)	μ (eV)	δ_{SP} (nm)	B_{SE} (nm)	B_{ET} (nm)
0.33	0.4	8.2	8.50	8.68
0.33	0.6	14.06	14.38	14.72
0.33	0.8	19.48	20.04	20.10
0.33	1.0	24.76	25.47	25.96

pair is moved further from the GM – increasing z – the ET function drops off exponentially, as the figure shows. The continuous lines in Fig. 6a represent fits of the calculated ET function (represented by symbols) with the exponential function $Ae^{-4z/B}$. The factor 4 in this expression has two sources: (i) the z distance of both donor and acceptor to the GM is varied and (ii) the ET function depends on the square of the field, see Eq. (12); each of these gives a doubling of the exponent, for a total of $2 \times 2 = 4$. Furthermore, because the donor-acceptor separation is kept constant at $x = 100$ nm, the free-space ET function is also constant and, hence, does not influence the exponential behavior. Table I shows the values of the parameter B_{ET} extracted from the fit, together with the analogous parameter B_{SE} extracted from fitting the SE dependence (the numerical factor in the exponent is 2 in this case, rather than 4, due to the fact that the SE rate depends linearly on the electric field; data not shown) and the penetration depth of the GP in the air above the graphene, calculated as $\delta_{\text{SP}} = 1/\text{Im}(k_z^{\text{SP}})$. As this table shows, the values of the parameters B_{SE} and B_{ET} match closely the calculated penetration depths of the GPs. This suggests that the main channel for enhancing the ET function between the QEs is the

GP resonance. As the separation between the two QEs becomes smaller and smaller, this relaxation channel becomes less and less important and the direct interaction dominates at distances below $x = 20$ nm, as panel 6b shows. In this panel we consider the influence of the in-plane distance between the donor and acceptor, for a fixed value of the chemical potential, $\mu = 0.4$ eV and fixed transition energy, $\hbar\omega = 0.33$ eV. We again fit the calculated ET function data (symbols) with the expression $Ae^{-4z/B}$. As one can see, above $x = 50$ nm the B_{ET} parameter extracted is very close to the penetration depth of the GP, δ_{SP} . When the donor and acceptor in-plane distance is smaller than $x = 50$ nm, the influence of the GP mode on the ET function is less profound, and, as the donor-acceptor pair is moved away from the GM, it recovers its free-space interaction at shorter distances. This is due to the fact that the influence of the homogeneous part of the Green's tensor dominates over the scattered part, cf Eq. A1; this effect will be further discussed in Sec. III C. In this section the quantity \mathcal{D} has the largest value of 0.48 for $\mu = 0.4$ eV, $\hbar\omega = 0.33$ eV at a donor-GM distance of 8 nm, confirming that the system is in the weak coupling regime.

C. Energy transfer efficiency

In the last section we investigated the SE and ET functions. When the donor dipole is excited it has two ways of relaxing to the ground state: it can either transfer its excitation energy to the acceptor dipole with an ET rate k_{ET} , or it can relax with decay rate k_{SE} , where it is assumed that there is no non-radiative decay, i.e. the intrinsic quantum yield of the donor is $Y_0 = 1$. The decay rate k_{SE} takes account of photon emission

into the far-field, coupling to GP modes and losses in the GM. The SE and ET processes are, therefore, in competition with each other and we introduce an energy transfer efficiency to describe this competition.

We define the energy transfer efficiency η as

$$\eta = \frac{k_{ET}}{k_{SE} + k_{ET}}. \quad (13)$$

This quantity gives the relative contribution of the energy transfer process to the total decay rate of the donor. If the ET efficiency, η , has a value $\eta > 50\%$, then the decay of the excited state of the donor occurs mainly by energy transfer to the acceptor, rather than relaxation into photon or GP modes.

We next consider a donor-acceptor pair. The donor emission and acceptor absorption spectra are both given by a Gaussian distribution

$$A_q e^{-(\lambda - \lambda_q)^2 / \Delta\lambda_q^2}, \quad (14)$$

where $q = D$ represents the donor and $q = A$ represents the acceptor. A_q is a normalization constant, λ_q gives the position of the spectral peak and $\Delta\lambda_q$ is related to the full width at half maximum (FWHM) of the spectrum. The donor emission peak and acceptor absorption maximum coincide at $\lambda_D = \lambda_A = 2 \mu\text{m}$. There are a variety of emitters at this wavelength, such as quantum dots and synthesized molecules.^{38,39} The normalization constant of the donor emission spectrum, $f_D(\lambda)$, is given as $A_D^{-1} = \int_0^\infty d\lambda f_D(\lambda)$. The width of the spectrum will be $\Delta\lambda_D = 20 \text{ nm}$, a reasonable value for a typical QE. The normalization constant for the acceptor absorption spectrum is $A_A = 0.021 \text{ nm}^2$, while the width is $\Delta\lambda_{Ai} = 50 \text{ nm}$.

The Förster radius, R_0 , is defined as the donor-acceptor separation at which the energy transfer efficiency η is 50%. The Förster radius can be calculated from the spectral overlap and has a value of 19 nm in free-space. R_0 is calculated from the spectral overlap of the normalized donor emission, f_D , and acceptor absorption, σ_A , spectra as

$$R_0 = \left[\frac{3c}{32\pi^4 n_r^4} \int_0^\infty d\lambda \lambda^2 f_D(\lambda) \sigma_A(\lambda) \right]^{1/6} \quad (15)$$

where n_r is the refractive index of the host medium, in our case air with $n_r = 1$.

In Fig. 7 we present contour plots of the ET efficiency for the donor-acceptor pair, with spectral properties described above; the donor and acceptor positions are fixed at $\mathbf{r}_D = (0, 0, 10 \text{ nm})$, and $\mathbf{r}_A = (x, 0, z)$, respectively. The chemical potential takes on two values, (7a) $\mu = 1.0 \text{ eV}$ and (7b) $\mu = 0.6 \text{ eV}$. When $\mu = 1.0 \text{ eV}$ the emission and absorption spectrum overlap strongly with the ET function. For this case the ET efficiency, η , has values above 70% even for separations along the GM as large as 100 nm, and the 50% efficiency distance is around 300 nm. This value is very large compared to the free-space Förster radius of $R_0 = 19 \text{ nm}$. When the value of the chemical potential is $\mu = 0.6 \text{ eV}$, the ET efficiency, η , has values above 50% for separations above 100 nm but now the overlap between the emission and absorption spectra and the ET function is poorer, thus showing a diminished

effect. The large confinement of light at the atomically thin GM surface can be used to efficiently transfer energy between a pair of QEs over large separations. Furthermore, this ET efficiency, η , can be controlled through gating of the GM, thus opening striking opportunities for possible applications, such as switching and sensing devices,^{24–26} light harvesting,²⁷ plasmonic rulers^{25,28} and quantum computing.²⁹

We next consider the behavior of the ET rate, k_{ET} , as a function of the in-plane separation between donor and acceptor. Figs. 8a and 8b show the ET rate, k_{ET} , as a function of the in-plane separation between the donor and acceptor, when their elevation above the GM is (a) $z_D = z_A = 5 \text{ nm}$ and (b) $z_D = z_A = 10 \text{ nm}$ on the same side of the GM. For both panels, we have fitted the near field with a Förster-type model, $(R_0/x)^n$, where R_0 is the Förster radius. At small separations the fit yields the values $n = 6$ typical of Förster ET, but we see that the Förster radius is modified from the free-space value. The fact that at small separations, $x < 10 \text{ nm}$, for $z_D = z_A = 5 \text{ nm}$ and $x < 20 \text{ nm}$, for $z_D = z_A = 10 \text{ nm}$, the ET rate, k_{ET} , follows an $n = 6$ dependence shows that the homogeneous part of the Green's tensor dominates, cf. (A1a), modified by the donor-acceptor interaction with the GM. Thus, there is an enhancement of the Förster radius, which depends on the donor-acceptor distances from the GM and the value of the chemical potential, μ . In Fig. 8a the Förster radius has a value of $R_0 = 30.7 \text{ nm}$ for chemical potential values $\mu = 0.8 \text{ eV}$ and $\mu = 1.0 \text{ eV}$. As the chemical potential value drops, the Förster radius decreases to $R_0 = 20.8 \text{ nm}$ for $\mu = 0.4 \text{ eV}$, approaching the free-space value of the Förster radius, $R_0 \approx 19 \text{ nm}$. The effect of tuning the Förster radius through the chemical potential is evident. In Fig. 8b the values of the Förster radius are smaller for the different values of the chemical potential, μ , due to the fact the QEs-GM distance is increased. When $\mu = 1.0 \text{ eV}$ we have the largest value of the Förster radius, $R_0 = 24.7 \text{ nm}$, due to our choice of the donor and acceptor. For the off-resonance case, $\mu = 0.4 \text{ eV}$, the Förster radius is approximately the free-space value, $R_0 \approx 19 \text{ nm}$.

At larger donor-acceptor separations, we use the following expression to fit the calculated ET rate

$$f(x) = \frac{A}{x} \exp\left(-\frac{2x}{B}\right), \quad (16)$$

which represents the dependence of the GP field intensity on the in-plane separation x (the factor 2 in the exponential results from the square of the Green's tensor, as does the x in the denominator – the GP field has a factor of $1/\sqrt{x}$). The fitting parameter B is tabulated in Table II, together with the corresponding propagation length of the GP along the interface of the GM, L_{SP} . As is clear, the correspondence between these parameters is very good indeed, confirming that, away from the near-field, the interaction between donor and acceptor occurs primarily through the GP excited by the donor at the surface of the GM. As we increase the distance between the QEs and the GM, the Förster regime dominates further away from the near-field, as can be seen from the fact that the intersection between the two fitting curves moves to larger distances. This is due to the small value of the penetration depth of the GP, $\delta_{SP} = 6.6 \text{ nm}$ at $\mu = 1.0 \text{ eV}$. In the next para-

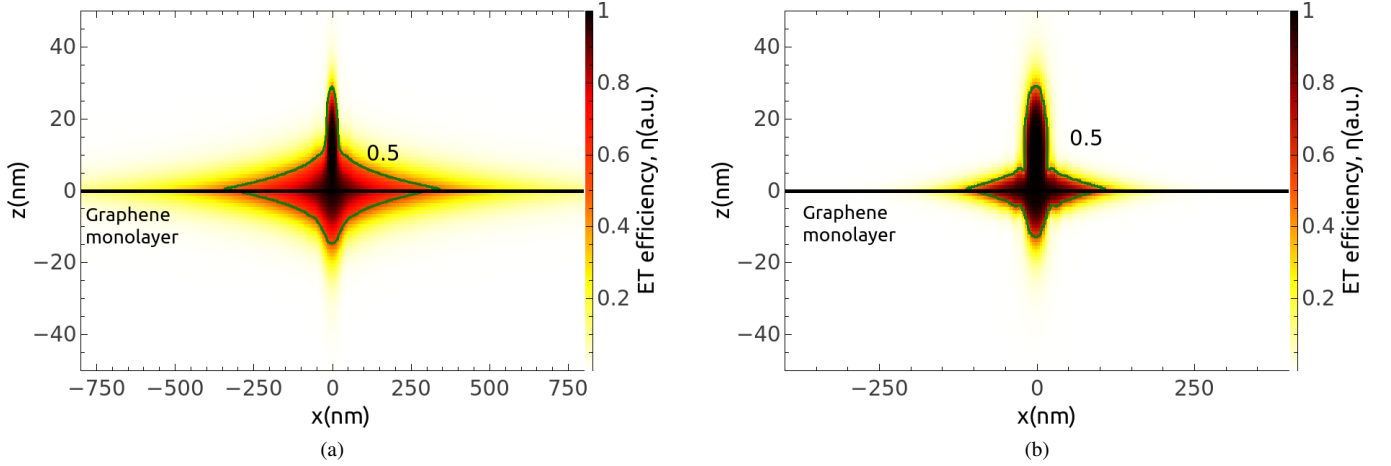


Figure 7: (Color online) Contour plot of the ET efficiency, η , between a pair of QEs, as a function of acceptor position for a fixed position of the donor at $\mathbf{r}_D = (0, 0, 10 \text{ nm})$ and different values of the chemical potential, (a) $\mu = 1 \text{ eV}$ and (b) $\mu = 0.6 \text{ eV}$. The green line gives the $\eta = 50\%$ values.

Table II:

$z \text{ (nm)}$	$\mu \text{ (eV)}$	$L_{SP} \text{ (nm)}$	$B \text{ (nm)}$
5	0.8	379.23	376.82
5	1.0	890.31	884.86
10	0.8	379.23	376.99
10	1.0	890.31	886.47

graph we will further consider the influence of the penetration depth to the ET rate, k_{ET} .

Figs. 8c and 8d consider the ET rate, k_{ET} , as a function of the donor-acceptor separation, for the case when the donor position is kept fixed at (8c) $z_D = 5 \text{ nm}$ and (8d) $z_D = 10 \text{ nm}$ above the GM, and the separation between the donor-acceptor, $d = z_D - z_A$ is varied, for $\mu = 1.0 \text{ eV}$ and $\mu = 0.4 \text{ eV}$. At small separations we again use the Förster model fitting presented earlier. To fit the behavior of the ET rate, k_{ET} , below the GM we choose the expression $f(z) = Ae^{-2z/B}$, where the parameter B will be connected with the penetration depth of the GP, δ_{SP} . In both figures, the GM position is denoted by the dashed vertical line. In Fig. 8c, for which the donor position is very close to the GM ($z_D = 5 \text{ nm}$), the behavior of the ET rate immediately below the GM is not trivial and comes from various contributions, such as direct interaction and GP-coupling. On the other hand, in panel 8d, for which $z_D = 10 \text{ nm}$, we can use the fitting function $f(z_A)$, and find for B the value $B = \delta_{SP} = 6.6 \text{ nm}$, showing that the main contribution to the ET rate comes from the GP on the GM. For the $\mu = 0.4 \text{ eV}$ case the ET rate, k_{ET} , is almost uninfluenced by the presence of the GM. The quantity \mathcal{D} has a maximum value of 0.2 for the donor-GM distance of 5 nm and $\mu = 1.0 \text{ eV}$.

IV. SUMMARY AND CONCLUSIONS

We have considered in this contribution the behavior of quantum systems placed near a free-standing graphene monolayer. The graphene monolayer can support graphene surface plasmon modes, tightly confined to the surface and having large propagation distances along the graphene monolayer.

We have begun by investigating the conditions of strong and weak coupling between a quantum system and the surface plasmon-polariton on the graphene monolayer. We have seen that for reasonably large values of the chemical potential $\mu > 0.4 \text{ eV}$ and any transition energies of the QE not in the THz regime, the weak coupling conditions are fulfilled. We can thus calculate such quantities as spontaneous emission and energy transfer functions. We have found that both of these quantities are enhanced, compared to their free space values, due to efficient coupling to the graphene plasmon modes.

Due to the competition of the donor-acceptor energy transfer process with other donor decay processes, we have defined the energy transfer efficiency, η , and have investigated the influence of the graphene plasmons on this quantity. We have shown that the energy transfer efficiency, η , can reach values above 50% for distances up to 300 nm along the graphene monolayer. This process can be controlled by tuning the value of the chemical potential, e.g. through gating.

Finally, we investigate the ET rate, k_{ET} , varying the donor-acceptor in-plane separation and distance from the GM, for various values of the chemical potential, μ . The ET rate, when the in-plane distance between the donor and acceptor is varied, has two major contributions: the Förster-type mechanism dominates at small separations, while the GP contribution dominates at large distances. The Förster-type ET rate follows a x^{-6} dependence, with an increased Förster radius value, due to the presence of the GM. The Förster radius value is increased from a free-space value of $R_0 = 19 \text{ nm}$, to

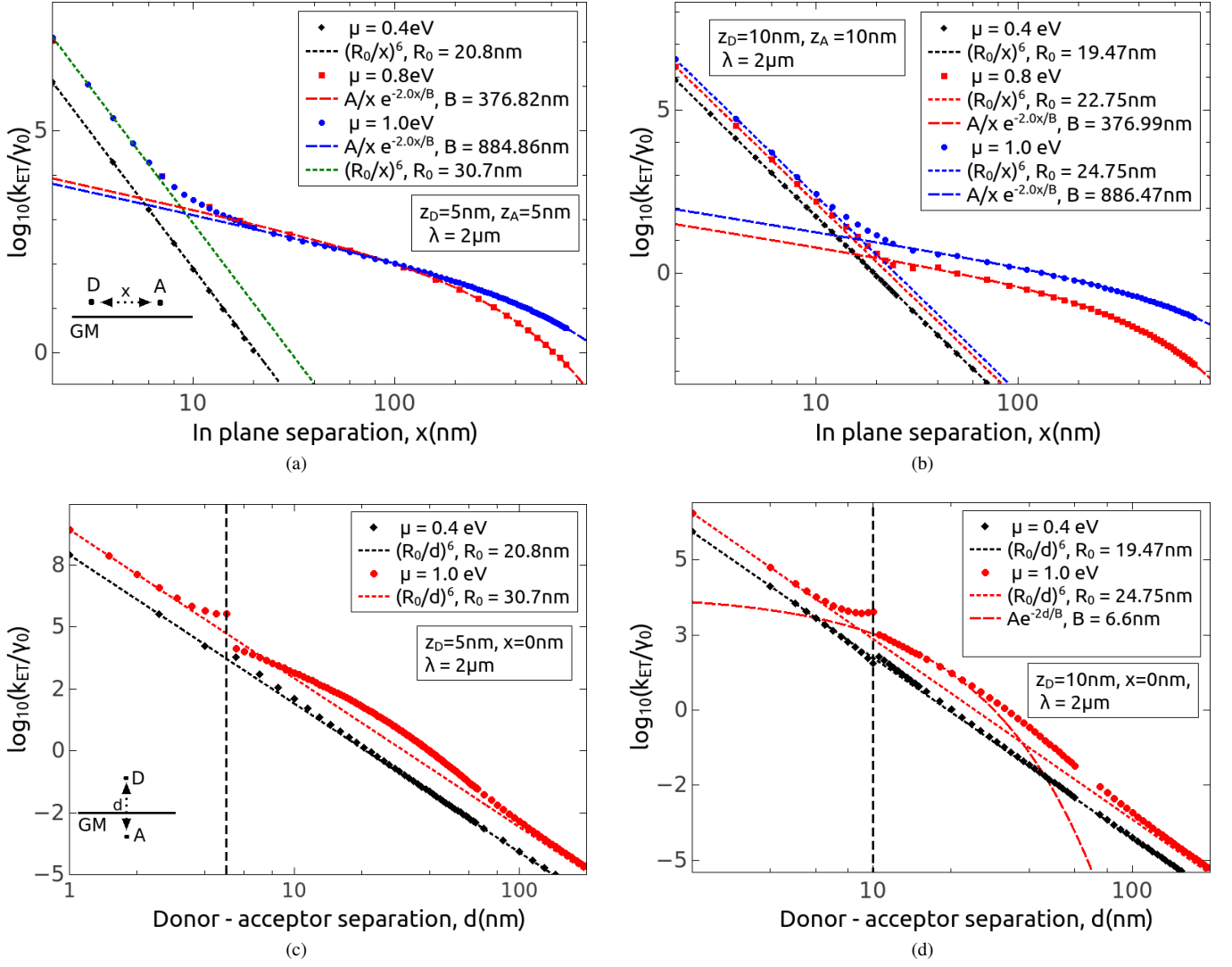


Figure 8: (Color online) (a-b) ET rate, k_{ET} , as a function of the donor-acceptor in-plane separation, x , for fixed donor positions, (a) $\mathbf{r}_D = (0, 0, 5 \text{ nm})$ and (b) $\mathbf{r}_D = (0, 0, 10 \text{ nm})$ respectively, and variable acceptor position, $\mathbf{r}_A = (x, 0, 5 \text{ nm})$ and $\mathbf{r}_A = (x, 0, 10 \text{ nm})$ respectively, for different values of the chemical potential, μ . (c-d) ET rate, k_{ET} , as a function of the donor-acceptor separation, d , for fixed donor positions, (c) $\mathbf{r}_D = (0, 0, 5 \text{ nm})$ and (d) $\mathbf{r}_D = (0, 0, 10 \text{ nm})$ respectively, and variable acceptor position $\mathbf{r}_A = (0, 0, z_A)$, with $d = z_D - z_A$ and for different values of the chemical potential, μ .

$R_0 = 30.7 \text{ nm}$ when $z_D = z_A = 5 \text{ nm}$ and $\mu = 1.0 \text{ eV}$. At larger distances, the main contribution comes from the GP propagation; the transition from the Förster to the GP-propagation mechanism depends on the distance of the donor-acceptor pair from the GM, and it occurs at donor-acceptor separations ranging from a few nm to a couple of tens of nm. When the z -distance between donor-acceptor is varied, for $x = 0$, the behavior is somewhat more complicated, but the GP penetration depth still dictates the interaction length. As the chemical potential, μ , decreases the ET rate approaches the free space values. Thus, by varying the value of the chemical potential, we can switch off the interaction channel or preferentially couple different species of donor-acceptor resonant pairs of QEs.

Acknowledgments

This work was supported by the Science Foundation Ireland under grant No. 10/IN.1/12975.

Appendix A: Green's tensor formalism

We will consider two planar half-spaces with different dielectric permittivities, ϵ_1 and ϵ_2 . The z -direction is perpendicular to the boundary between the two half-spaces. In order to calculate the Green's tensor for this system, we use the method of scattering superposition.⁴⁰ The Green's tensor has

the form

$$\mathfrak{G}^{(11)}(\mathbf{r}, \mathbf{s}, \omega) = \mathfrak{G}_h^{(11)}(\mathbf{r}, \mathbf{s}, \omega) + \mathfrak{G}_s^{(11)}(\mathbf{r}, \mathbf{s}, \omega), \quad (\text{A1a})$$

$$\mathfrak{G}^{(21)}(\mathbf{r}, \mathbf{s}, \omega) = \mathfrak{G}_s^{(21)}(\mathbf{r}, \mathbf{s}, \omega), \quad (\text{A1b})$$

where the first of the two labels in the superscript ($i1$) denotes the field point, while the second denotes the source point. The

subscript s denotes the scattering term, always present, while the homogeneous term $\mathfrak{G}_h^{(11)}(\mathbf{r}, \mathbf{s}, \omega)$ contributes only when the source and field points are in the same medium.

The scattering terms have the following expression

$$\mathfrak{G}_s^{(11)}(\mathbf{r}, \mathbf{s}, \omega) = \frac{i}{8\pi^2} \sum_K \int d^2k_\rho \frac{1}{k_{z1}k_\rho^2} R_K^{+11-} \mathbf{K}(k_\rho, k_{z1}, \mathbf{r}) \otimes \mathbf{K}^*(k_\rho, -k_{z1}, \mathbf{s}) \quad (\text{A2a})$$

$$\mathfrak{G}_s^{(21)}(\mathbf{r}, \mathbf{s}, \omega) = \frac{i}{8\pi^2} \sum_K \int d^2k_\rho \frac{1}{k_{z1}k_\rho^2} R_K^{-11-} \mathbf{K}(k_\rho, -k_{z2}, \mathbf{r}) \otimes \mathbf{K}^*(k_\rho, -k_{z1}, \mathbf{s}) \quad (\text{A2b})$$

where $k_\rho = \sqrt{k_i^2 - k_{zi}^2}$ is the in-plane propagation constant, k_{zi} is the perpendicular propagation constant in medium i , and $k_i = \frac{\omega}{c} \sqrt{\epsilon_i}$ is the wavenumber in medium i ($i = 1, 2$). The above expressions involve a summation over \mathbf{K} which represents \mathbf{M} and \mathbf{N} , or the transverse electric (TE) and transverse magnetic (TM) modes.

We impose the following continuity conditions at the boundary between the two half spaces, $z = 0$,

$$\hat{\mathbf{z}} \times [\mathfrak{G}^{(11)}(\mathbf{r}, \mathbf{s}, \omega) - \mathfrak{G}^{(21)}(\mathbf{r}, \mathbf{s}, \omega)]_{z=0} = 0, \quad (\text{A3a})$$

$$\hat{\mathbf{z}} \times [\nabla \times \mathfrak{G}^{(11)}(\mathbf{r}, \mathbf{s}, \omega) - \nabla \times \mathfrak{G}^{(21)}(\mathbf{r}, \mathbf{s}, \omega)]_{z=0} = -i \frac{4\pi}{c} k_0 \sigma \hat{\mathbf{z}} \times \mathfrak{G}^{(21)}(\mathbf{r}, \mathbf{s}, \omega), \quad (\text{A3b})$$

where σ is the surface conductivity.

Using Eqs. (A2) in (A3) we obtain the generalized Fresnel coefficients, which have the form,^{13,41}

$$R_M^{11} = \frac{k_{z1} - k_{z2} - 2\alpha k_0}{k_{z1} + k_{z2} + 2\alpha k_0}, \quad R_N^{11} = \frac{k_2^2 k_{z1} - k_1^2 k_{z2} + 2\alpha k_0 k_{z1} k_{z2}}{k_2^2 k_{z1} + k_1^2 k_{z2} + 2\alpha k_0 k_{z1} k_{z2}} \quad (\text{A4a})$$

$$R_M^{21} = \frac{2k_{z1}}{k_{z1} + k_{z2} + 2\alpha k_0}, \quad R_N^{21} = \frac{2k_1 k_2 k_{z1}}{k_2^2 k_{z1} + k_1^2 k_{z2} + 2\alpha k_0 k_{z1} k_{z2}}, \quad (\text{A4b})$$

where $\alpha = 2\pi\sigma/c$.

Appendix B: Spontaneous Emission and Energy Transfer Rates

The spontaneous emission function γ has the form:^{42,43}

$$\gamma(\mathbf{r}, \omega) = \frac{2\omega^2 \mu^2}{\hbar \epsilon_0 c^2} \text{Im} [\mathbf{n}_\mu \cdot \mathfrak{G}(\mathbf{r}, \mathbf{r}, \omega) \cdot \mathbf{n}_\mu], \quad (\text{B1})$$

where \mathbf{n}_μ is a unit vector along the direction of the transition dipole moment of the emitter, μ , and $\mathfrak{G}(\mathbf{r}, \mathbf{r}, \omega)$ is the Green's tensor introduced in Appendix A.

A useful quantity to introduce is the normalized SE rate, defined as

$$\tilde{\gamma} = \frac{\gamma}{\gamma_0} = n_i + \frac{6\pi c}{\omega} \text{Im} [\mathbf{n}_\mu \cdot \mathfrak{G}_s(\mathbf{r}, \mathbf{r}, \omega) \cdot \mathbf{n}_\mu], \quad (\text{B2})$$

where the expression for γ_0 is given by the Einstein A-coefficient as $\gamma_0 = \omega^3 \mu^2 / (3\pi \hbar \epsilon_0 c^3)$. The subscript s on the Green's tensor denotes the scattering part of this quantity, which we introduced in Eqs. (A1) and $n_i = \sqrt{\epsilon_i}$ is the refractive index of the medium into which the quantum system is embedded. The normalized SE rate gives either an enhancement ($\tilde{\gamma} > 1$) or a reduction ($\tilde{\gamma} < 1$) of the SE rate compared to its free-space value, γ_0 .

When dealing with statistical ensembles of emitters, the emission spectrum will be different from that of a single emitter, which we have taken to have a δ -shape. The emission rate for the ensemble can then be expressed as:

$$k_{\text{SE}} = \int_0^\infty d\lambda f_D(\lambda) \gamma(\lambda), \quad (\text{B3})$$

where $f_D(\lambda)$ is the area-normalized emission spectrum of the emitter, with $\int_0^\infty d\lambda f_D(\lambda) = 1$.

Furthermore, we introduce the ET function, Γ , between a donor-acceptor pair, which has the form²³

$$\Gamma(\mathbf{r}_A, \mathbf{r}_D, \omega) = \frac{2\pi}{\hbar^2} \left(\frac{\omega^2}{c^2 \epsilon_0} \right)^2 |\boldsymbol{\mu}_A \cdot \mathfrak{G}(\mathbf{r}_A, \mathbf{r}_D, \omega) \cdot \boldsymbol{\mu}_D|^2, \quad (\text{B4})$$

where again $\mathfrak{G}(\mathbf{r}_A, \mathbf{r}_D, \omega)$ is the Green's tensor for the particular geometry, $\mathbf{r}_{D(A)}$ is the position of the donor D (acceptor A) and $\boldsymbol{\mu}_{D(A)}$ is the transition dipole moment of the donor D (acceptor A). The above expression for the energy transfer function depends on the donor-acceptor pair through the emission frequency of the donor and the transition dipole moment of the donor and acceptor. The influence of the geometry is completely encapsulated in the Green's tensor, being proportional to the electric field intensity, through the square of the Green's tensor.

To consider only the influence of the geometry on a general donor-acceptor pair, we now introduce the normalized ET function for the system, $\tilde{\Gamma}$, defined as

$$\tilde{\Gamma}(\omega) = \frac{\Gamma(\omega)}{\Gamma_0(\omega)} = \frac{|\mathbf{n}_A \cdot \mathfrak{G}(\mathbf{r}_A, \mathbf{r}_D, \omega) \cdot \mathbf{n}_D|^2}{|\mathbf{n}_A \cdot \mathfrak{G}_0(\mathbf{r}_A, \mathbf{r}_D, \omega) \cdot \mathbf{n}_D|^2}, \quad (\text{B5})$$

where $\mathfrak{G}_0(\mathbf{r}_A, \mathbf{r}_D, \omega)$ is the Green's tensor in free space and $\mathbf{n}_{D(A)}$ is a unit vector in the direction of $\boldsymbol{\mu}_{D(A)}$.

Analogously to the case of the SE rate, when considering statistical ensembles of donors and acceptors, the donor emission spectrum $f_D(\lambda)$ and acceptor absorption cross-section $\sigma_A(\lambda)$ need to be taken into account when calculating the energy transfer rate. We, therefore, have:⁴⁴

$$k_{\text{ET}} = 36\pi^2 Y_D k_{\text{SE}} \int_0^\infty \frac{d\lambda}{\lambda^2} f_D(\lambda) |\mathbf{n}_A \cdot \mathfrak{G}(\mathbf{r}_A, \mathbf{r}_D, \lambda) \cdot \mathbf{n}_D|^2 \sigma_A(\lambda), \quad (\text{B6})$$

where Y_D is the intrinsic quantum yield of the donor. We have used this expression to calculate the energy transfer rate between donors and acceptors with specific emission and absorption spectra and to investigate how the energy transfer process competes with the emission process of the donor.

-
- ¹ W. L. Barnes, A. Dereux, and T. W. Ebbesen, *Nature* **424**, 824 (2003).
 - ² J.A. Dionne, L.A. Sweatlock, H.A. Atwater, and A. Polman, *Phys. Rev. B* **72**, 075405 (2005).
 - ³ F. J. García de Abajo, *ACS Photonics* **1**, 135 (2014).
 - ⁴ A. N. Grigorenko, M. Polini, and K. S. Novoselov, *Nat. Phot.* **6**, 749 (2012).
 - ⁵ P. Alonso-González, A. Y. Nikitin, F. Golmar, A. Centeno, A. Pesquera, S. Vélez, J. Chen, G. Navickaite, F. Koppens, A. Zurutuza, F. Casanova, L. E. Hueso, and R. Hillenbrand, *Science* **344**, 1369 (2014).
 - ⁶ Y. V. Bludov, A. Ferreira, N. M. R. Peres, and M. I. Vasilevskiy, *Int. J. Mod. Phys. B* **27**, 1341001 (2013).
 - ⁷ T. Low and P. Avouris, *ACS Nano* **8**, 1086 (2014).
 - ⁸ A. H. Castro Neto, N. M. R. Peres, K. S. Novoselov, and A. K. Geim, *Rev. Mod. Phys.* **81**, 109 (2009).
 - ⁹ R. R. Nair, P. Blake, A. N. Grigorenko, K. S. Novoselov, T. J. Booth, T. Stauber, N. M. R. Peres, and A. K. Geim, *Science* **320**, 1308 (2008).
 - ¹⁰ S. Thongrattanasiri, F. H. L. Koppens, and F. J. García de Abajo, *Phys. Rev. Lett.* **108**, 047401 (2012).
 - ¹¹ V. W. Brar, M. S. Jang, M. Sherrott, J. J. Lopez, and H. A. Atwater, *Nano Lett.* **13**, 2541 (2013).
 - ¹² A. Y. Nikitin, F. Guinea, F. J. García-Vidal, and L. Martín-Moreno, *Phys. Rev. B* **85**, 081405 (2012).
 - ¹³ G. W. Hanson, *J. Appl. Phys.* **103**, 064302 (2008).
 - ¹⁴ A. Y. Nikitin, F. Guinea, F. J. García-Vidal, and L. Martín-Moreno, *Phys. Rev. B* **84**, 195446 (2011).
 - ¹⁵ F. H. L. Koppens, D. E. Chang, and F. J. García de Abajo, *Nano Lett.* **11**, 3370 (2011).
 - ¹⁶ J. Tisler, T. Oeckinghaus, R. J. Stöhr, R. Kolesov, R. Reuter, F. Reinhard, and J. Wrachtrup, *Nano Lett.* **13**, 3152 (2013).
 - ¹⁷ G. Konstantatos, M. Badioli, L. Gaudreau, J. Osmond, M. Bernechea, F. P. Garcia de Arquer, F. Gatti, and F. H. L. Koppens, *Nat. Nanotechnol.* **7**, 363 (2012).
 - ¹⁸ A. Manjavacas, S. Thongrattanasiri, D. E. Chang, and F. J. García de Abajo, *New J. Phys.* **14**, 123020 (2012).
 - ¹⁹ A. Gonzalez-Tudela, D. Martín-Cano, E. Moreno, L. Martín-Moreno, C. Tejedor, and F. J. García-Vidal, *Phys. Rev. Lett.* **106**, 020501 (2011).
 - ²⁰ D. Dzsojtan, A. S. Sørensen, and M. Fleischhauer, *Phys. Rev. B* **82**, 075427 (2010).
 - ²¹ P. A. Huidobro, A. Y. Nikitin, C. González-Ballester, L. Martín-Moreno, and F. J. García-Vidal, *Phys. Rev. B* **85**, 155438 (2012).
 - ²² S.-A. Biehs and G. S. Agarwal, *Appl. Phys. Lett.* **103**, 243112 (2013).
 - ²³ H.T. Dung, L. Knöll, and D.-G. Welsch, *Phys. Rev. A* **65**, 043813 (2002).
 - ²⁴ F. Schwierz, *Nat. Nanotechnol.* **5**, 487 (2010).
 - ²⁵ G. Mazzamuto, A. Tabani, S. Pazzagli, S. Rizvi, A. Reserbat-Plantey, K. Schädler, G. Navickaite, L. Gaudreau, F. S. Cataliotti, F. Koppens, and C. Toninelli, *New J. Phys.* **16**, 113007 (2014).
 - ²⁶ Q. He, S. Wu, Z. Yin, and H. Zhang, *Chem. Sci.* **3**, 1764 (2012).
 - ²⁷ C.-C. Lin, D.-Y. Wang, K.-H. Tu, Y.-T. Jiang, M.-H. Hsieh, C.-C. Chen, and C.-W. Chen, *Appl. Phys. Lett.* **98**, 263509 (2011).
 - ²⁸ Y. Wang, Z. Li, J. Wang, J. Li, and Y. Lin, *Trends in Biotechnology* **29**, 205 (2011).
 - ²⁹ M. J. Gullans and J. M. Taylor, *arXiv:1407.7035 [cond-mat.mes-hall]* (2014).
 - ³⁰ M. Jablan, H. Buljan, and M. Soljačić, *Phys. Rev. B* **80**, 245435 (2009).
 - ³¹ B. Wunsch, T. Stauber, F. Sols, and F. Guinea, *New Journ. Phys.* **8**, 318 (2006).
 - ³² L. A. Falkovsky, *J. Phys.: Conference Series* **129**, 012004 (2008).
 - ³³ K. S. Novoselov, A. K. Geim, S. V. Morozov, D. Jiang, Y. Zhang, S. V. Dubonos, I. V. Grigorieva, and A. A. Firsov, *Science* **306**, 666 (2004).
 - ³⁴ K. S. Novoselov, A. K. Geim, S. V. Morozov, D. Jiang, M. I. Katsnelson, I. V. Grigorieva, S. V. Dubonos, and A. A. Firsov, *Nature* **438**, 197 (2005).

- ³⁵ P. Törmä and W. L. Barnes, arXiv:1405.1661v1 [physics.optics] (2014).
- ³⁶ T. Hümmer, F.J. García-Vidal, L. Martín-Moreno, and D. Zueco, Phys. Rev. B **87**, 115419 (2013).
- ³⁷ L.C. Andreani, G. Panzarini, and J.-M. Gérard, Phys. Rev. B **60**, 13276 (1999).
- ³⁸ J. M. Pietryga, R. D. Schaller, D. Werder, M. H. Stewart, V. I. Klimov, and J. A. Hollingsworth, J. Am. Chem. Soc. **126**, 11752 (2004).
- ³⁹ J. A. Treadway, G. F. Strouse, R. R. Ruminski, and T. J. Meyer, Inor. Chem. **40**, 4508 (2001).
- ⁴⁰ W. C. Chew, *Waves and Fields in Inhomogeneous Media* (IEEE Press, New York, NY, USA, 1995).
- ⁴¹ A. Y. Nikitin, F. J. García-Vidal, and L. Martín-Moreno, IEEE J. Select. Topics Quantum Electron. **19**, 4600611 (2013).
- ⁴² H.T. Dung, L. Knöll, and D.-G. Welsch, Phys. Rev. A **57**, 3931 (1998).
- ⁴³ H.T. Dung, L. Knöll, and D.-G. Welsch, Phys. Rev. A **62**, 053804 (2000).
- ⁴⁴ X. Zhang, C. A. Marocico, M. Lunz, V. A. Gerard, Y. K. Gun'ko, V. Lesnyak, N. Gaponik, A. S. Susha, A. L. Rogach, and A. L. Bradley, ACS Nano **8**, 1273 (2014).